

# Enhanced Deoxygenation of Solvents via an Improved Inert Gas Bubbling Method with a Ventilation Pathway

Dongcheol Park, Seong Min Won, and Hohjai Lee\*



Cite This: <https://doi.org/10.1021/acsomega.4c05786>



Read Online

ACCESS |



Metrics & More

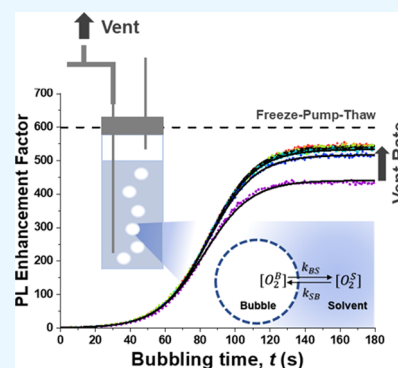


Article Recommendations



Supporting Information

**ABSTRACT:** We introduce an improved inert gas bubbling method for solvent deoxygenation, featuring a ventilation path alongside the inert gas inlet to enhance the efficiency and reproducibility. While essential for life, oxygen's reactivity can disrupt scientific and industrial processes by forming unwanted intermediates and deactivating catalysts, necessitating efficient deoxygenation methods. Traditional methods like freeze–pump–thaw (FPT) are effective but time-consuming, require stringent safety measures, and have potential limitations for use with aqueous and biological samples. Our enhanced inert gas bubbling method retains the simplicity and safety of conventional bubbling while achieving FPT-like deoxygenation efficiency, demonstrated by photoluminescence intensity and lifetime measurements in acetonitrile (ACN) and toluene (TOL). Simulations using a simplified kinetic model and the Stern–Volmer equation reveal that the added ventilation pathway reduces oxygen contamination in Ar gas bubbles, improving the deoxygenation efficiency. This method is widely applicable in academic and industrial fields, requiring consistent and efficient solvent deoxygenation.



## 1. INTRODUCTION

The oxygen molecule is a crucial component for life on this planet, constituting 21% of the air. However, it also plays an adverse role in human activities. Oxygen accelerates the cellular aging process through the formation of reactive oxygen species.<sup>1–3</sup> Chemists often struggle to maintain an O<sub>2</sub>-free environment<sup>4–7</sup> because oxygen readily forms unwanted intermediates with radicals or anions during reactions.<sup>8–14</sup> It also associates with transition metals, leading to the deactivation of transition metal-containing catalysts.<sup>15–18</sup> These interactions are particularly detrimental in fluorescence microscopy and single-molecule fluorescence spectroscopy, where O<sub>2</sub> not only suppresses fluorescence emission<sup>19</sup> but also causes photobleaching and photodamage of fluorophores.<sup>20,21</sup> In material science, O<sub>2</sub> adsorption on a metal substrate causes defects in thin film, hindering large-scale production.<sup>22–26</sup> Organic optoelectronic devices, including organic photovoltaic (OPV) cells and organic light-emitting diode (OLED) devices, suffer from intrinsic decay of active materials due to reactions with O<sub>2</sub>.<sup>27–33</sup> Therefore, the efficient deoxygenation of samples remains a critical challenge in both academic and industrial settings.

Dissolved O<sub>2</sub> removal from solvents is a common laboratory process with several methods available: boiling, sonication, freeze–pump–thaw (FPT), bubbling of inert gas (Ar or N<sub>2</sub>), and the addition of O<sub>2</sub> scavengers.<sup>4,7,34–40</sup> Among them, FPT and inert gas bubbling methods are most frequently practiced. FPT is known for its high performance and rigor. This method involves a cold reservoir like liquid N<sub>2</sub> to freeze solvents and a high-performance vacuum pump for degassing. A single FPT

cycle takes approximately 30 min to prepare a sample for a standard 1 cm × 1 cm spectroscopic cuvette, and multiple (more than three) cycles are recommended for optimal performance. Spending an hour or more on FPT deoxygenation is a common practice. Special safety precautions are required during thawing, as sudden volume expansion of the solvent can be hazardous.<sup>35</sup> FPT is not ideal for aqueous solutions and biological systems because freezing and thawing can disrupt tissue, cell, organelle, and protein structures due to extreme temperature changes. Water expansion at low temperatures also makes the FPT problematic for aqueous media.

In contrast, inert gas bubbling offers simplicity, relative safety, and applicability to biological and aqueous samples. As illustrated in Figure 1a, a typical gas bubbling setup includes a high-purity inert gas tank (>99.999%), a regulator, and a tube ending in a needle. Inert gas bubbles generated at the needle's tip, immersed in the solvent, facilitate O<sub>2</sub> removal. The sample container is capped with an exhaust line to prevent pressure buildup. Bubbling duration depends on experimental parameters, such as solvent type and quantity, tube material, and the desired deoxygenation level. A low gas inlet flow rate ( $R_{in}$ )

**Received:** June 21, 2024

**Revised:** September 28, 2024

**Accepted:** October 3, 2024

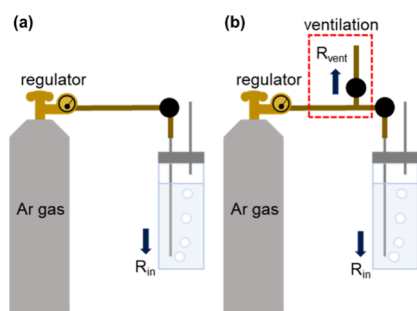


**Figure 1.** Schematic diagrams for (a) a conventional inert gas bubbling setup and (b) the improved setup used in this work featuring a ventilation pathway (red dashed box). Solid black circle: mass flow controller (MFC), black arrow: Ar gas flow direction. The setup with  $R_{\text{vent}} = 0$  in (b) is equivalent to the setup in (a).

leads to slow deoxygenation, while a high flow rate can cause rapid solvent vaporization, compromising experiments requiring precise concentration control. Excessive  $R_{\text{in}}$  can also cause pressure accumulation within the container if it is not adequately exhausted. In this study, we maintained a moderate  $R_{\text{in}}$  of 20 standard cubic centimeters per minute (sccm), as demonstrated in Supporting Video S1.

Pagano et al. quantitatively studied deoxygenation in cyclohexane by measuring fluorescence intensity enhancements of polyaromatic hydrocarbons with  $\text{N}_2$  bubbling (enhancement factors of 3.61, 4.17, 7.63, and 21.81 for chrysene, phenanthrene, naphthalene, and pyrene, respectively).<sup>36</sup> They accounted for solvent loss ( $\sim 0.07\%$ /min) during bubbling and a static and dynamic quenching effect to obtain the enhancement factors with real-time simultaneous measurements of steady-state fluorescence intensity, absorption, fluorescence lifetime, and dissolved  $\text{O}_2$  level.<sup>41</sup>

Although inert gas bubbling is well-known for its simplicity, cost-effectiveness, and safety, its shortcomings include low reproducibility and limited effectiveness in  $\text{O}_2$  removal. Addressing this, we present an improved inert gas bubbling method that reproducibly deoxygenates two common organic solvents, acetonitrile (ACN) and toluene (TOL), to levels comparable to the FPT method. This improved method maintains the same deoxygenation speed and the advantages of the traditional setup with a minimal adjustment: the addition of a ventilation pathway. Simulation using a simplified kinetic model and the Stern–Volmer equation reveal that this ventilation mitigates ‘ $\text{O}_2$  contamination’ in inert gas bubbles, enhancing the method’s efficacy and reliability.

## 2. RESULTS AND DISCUSSION

The bubbling process was carried out using the improved setup, as shown in Figure 1b. The primary improvement was the addition of a ventilation path next to the inlet needle (outlined by a red dashed line) compared to the conventional setup in Figure 1a. The inlet flow rate ( $R_{\text{in}}$ ) and ventilation flow rate ( $R_{\text{vent}}$ ) were precisely controlled using mass flow controllers (MFCs). The improved configuration was inspired by the standard Schlenk line setup with a one-way ventilation, oil (or mercury) bubbler.<sup>35</sup> In this study, however, we systematically controlled the ventilation flow rate using the MFC to quantitatively investigate the details of the ventilation path effect. It should be noted that the improved setup in Figure 1b with  $R_{\text{vent}} = 0$  is essentially equivalent to the conventional setup shown in Figure 1a. The extent of

deoxygenation in the solvent was quantified by real-time monitoring of the photoluminescence (PL) of platinum(II) octaethylporphyrin (PtOEP). PtOEP was chosen as an  $\text{O}_2$  indicator because its luminescence is predominantly phosphorescence, which is more sensitive to  $\text{O}_2$  concentration than fluorescence due to its longer lifetime.<sup>6,42</sup>

As depicted in Figure 2, PtOEP exhibits absorption peaks at 375, 500, and 540 nm and a phosphorescence band between

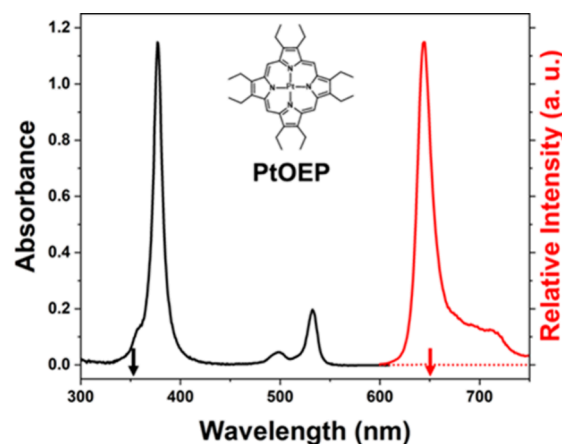


**Figure 2.** Absorption (solid black line) and photoluminescence (PL) (solid red line, excited at 355 nm) spectra of 5  $\mu\text{M}$  PtOEP in ACN. Note that the PL intensity after Ar gas bubbling is approximately 500 times stronger than that before bubbling (red dashed line). Black and red arrows indicate the excitation wavelength ( $\lambda_{\text{exc}} = 355$  nm) and the detection wavelength ( $\lambda_{\text{em}} = 650$  nm) for the photoluminescence enhancement factor (PLEF) measurement, respectively.

600 and 750 nm, which is dramatically quenched in the presence of  $\text{O}_2$ .<sup>42</sup> We measured the photoluminescence enhancement factor,  $\text{PLEF}(R_{\text{vent}}, t) = \frac{I(R_{\text{vent}}, t)}{I_0}$ , where  $I(R_{\text{vent}}, t)$  represents the PL intensity of the PtOEP solution at 650 nm under 355 nm continuous-wave photoexcitation at a specific bubbling time  $t$  and ventilation flow rate  $R_{\text{vent}}$  using the experimental setup shown in Figure S1a.  $I_0$  is the PL intensity of the air-saturated PtOEP solution before Ar-gas bubbling. The concentration of the PtOEP solution used in all measurements in this work was 5  $\mu\text{M}$ .

To explore the influence of ventilation flow rate  $R_{\text{vent}}$  on deoxygenation, PLEF was monitored at various ventilation rates ( $R_{\text{vent}} = 0, 50, 100, 200, 300$ , and 400 sccm). Real-time PLEF profiles were obtained by performing at least three independent measurements (Figure S2) and averaging the results, as shown in Figure 3. The PLEF profiles exhibit a sigmoidal increase, characterized by an induction period followed by an inflection point around 90 s and a plateau beyond 140 s. The values in the plateau range were averaged to obtain the enhancement factor for the fully bubbled sample,  $\text{PLEF}(R_{\text{vent}}, \infty)$ . In ACN,  $\text{PLEF}(R_{\text{vent}}, \infty)$  increases to 433.3, 515.3, 533.7, 541.0, 543.5, and 546.2 as  $R_{\text{vent}}$  increases, saturating around 400 sccm (Table S1). The ventilation effect (VE), representing the percentage increase in PLEF due to ventilation compared to no ventilation (i.e., the conventional configuration in Figure 1a), is estimated using the formula  $\text{VE} = \frac{\text{PLEF}(400\text{sccm}, \infty) - \text{PLEF}(0\text{sccm}, \infty)}{\text{PLEF}(0\text{sccm}, \infty)} \times 100 (\%)$  and is calculated to be 26.0%. As a reference, the PLEFs of the FPT-treated samples were assessed separately (black dashed lines in

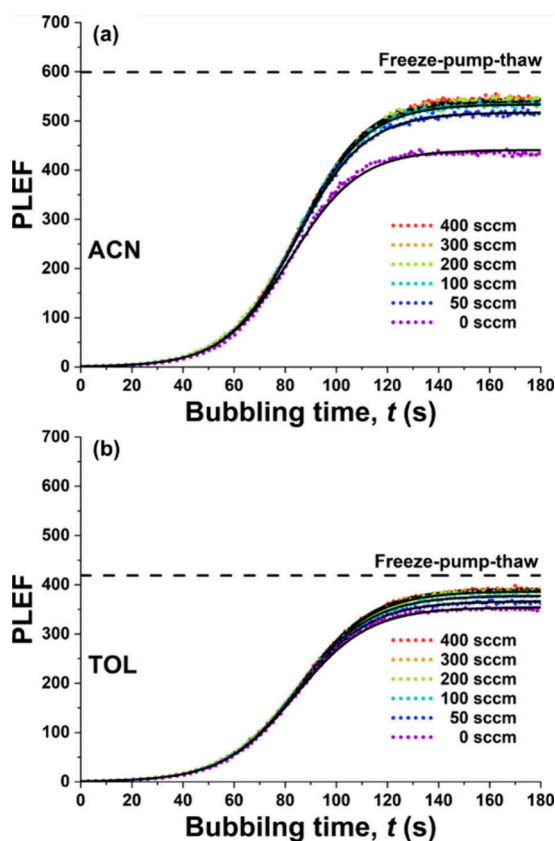


**Figure 3.** Experimental (averaged over 3 replicas, colored dot) and simulated (black line) photoluminescence enhancement factor (PLEF) profiles of a 5  $\mu\text{M}$  PtOEP solution in (a) ACN and (b) TOL against Ar gas bubbling time,  $t$ , at different  $R_{\text{vent}}$ . The black dashed lines indicate the PLEF values of the FPT-treated samples. Note that measurement with  $R_{\text{vent}} = 0$  sccm is equivalent to that in the conventional setup.

**Figure 3,**  $\text{PLEF}(\text{FPT})_{\text{ACN}} = 599.1$ ,  $\text{PLEF}(\text{FPT})_{\text{TOL}} = 418.9$ . The ratio  $\frac{\text{PLEF}(400\text{sccm}, \infty)}{\text{PLEF}(\text{FPT})}$  reaches 0.91 in ACN, demonstrating that the deoxygenation performance of the Ar bubbling method, when coupled with the ventilation path, closely approaches that of the rigorous FPT method. A similar trend is observed in TOL (Table S2), where VE is 12.1% and the ratio  $\frac{\text{PLEF}(400\text{sccm}, \infty)}{\text{PLEF}(\text{FPT})} = 0.94$ .  $\text{PLEF}(R_{\text{vent}}, \infty)$  values in TOL are 20–30% lower than those in ACN, which can be attributed to the higher oxygen solubility in TOL compared to ACN.<sup>7,36,41,43</sup> Notably,  $\text{PLEF}(R_{\text{vent}}, \infty)$  values exhibit high reproducibility, with standard deviations of less than 1% in ACN and less than 1.7% in TOL (Tables S1 and S2).

To verify whether the increased PL intensities in Figure 3 result from a decrease in the concentration of the  $\text{O}_2$  rather than an increase in the PtOEP concentration due to solvent evaporation during Ar-gas bubbling, we measured  $\text{PLEF}(R_{\text{vent}}, \infty)$  using the PL lifetime of PtOEP, as described in Figure S1b. The PL lifetime is insensitive to the PtOEP concentration but sensitive to the amount of quencher, namely,  $\text{O}_2$ . In this case, the photoluminescence enhancement can be expressed as  $\text{PLEF}(R_{\text{vent}}, \infty) = \frac{\tau(R_{\text{vent}}, \infty)}{\tau_0}$ , where  $\tau(R_{\text{vent}}, \infty)$  and  $\tau_0$  are corresponding to the PL lifetimes of the sample fully bubbled at  $R_{\text{vent}}$  and before bubbling ( $\tau_{0,\text{ACN}} = 179$  ns,  $\tau_{0,\text{TOL}} = 229$  ns, Figure S4), respectively. Figure S5 displays the three sets of

time-resolved PtOEP PL decay profiles, with monoexponential decay fitting results summarized in Tables S3 and S4 for ACN and TOL, respectively. It is clearly shown that the PL lifetime increases as  $R_{\text{vent}}$  increases for both solvents. Moreover, the  $\text{PLEF}(R_{\text{vent}}, \infty)$  values obtained through PL intensity and PL lifetime measurements are closely aligned with each other across all  $R_{\text{vent}}$  values for both ACN and TOL (Figure 4).

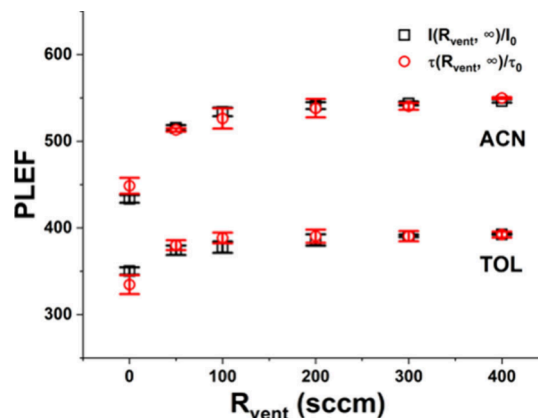


**Figure 4.** Photoluminescence enhancement factor (PLEF) values obtained by the PL intensity ( $I(R_{\text{vent}}, \infty)/I_0$ , black square) and PL lifetime ( $\tau(R_{\text{vent}}, \infty)/\tau_0$ , red circle) at different ventilation flow rates  $R_{\text{vent}}$  in ACN (upper plots) and TOL (lower plots).  $I_0$  and  $\tau_0$  are the PL intensity and lifetime, respectively, before Ar-gas bubbling, repeated three times ( $n = 3$ ). Note that measurement with  $R_{\text{vent}} = 0$  sccm is equivalent to that in the conventional setup.

Therefore, we confirm that the increase in PLEF observed in Figure 3 dominantly stems from the decrease in the dissolved  $\text{O}_2$  concentration rather than the increase in the PtOEP concentration due to solvent evaporation during bubbling. Figure S6 compares the PL lifetimes of the samples deoxygenated by Ar-gas bubbling at  $R_{\text{vent}} = 400$  sccm and those deoxygenated by the FPT method. The resulting PLEF ratios,  $\frac{\text{PLEF}(400\text{sccm}, \infty)}{\text{PLEF}(\text{FPT})} = \frac{\tau_{400\text{sccm}}}{\tau_{\text{FPT}}}$ , are 0.94 (98  $\mu\text{s}/104$   $\mu\text{s}$ ) for ACN and 0.93 (89  $\mu\text{s}/95$   $\mu\text{s}$ ) for TOL. These values are in good agreement with the PLEF ratio values obtained above by the PL intensity.

How can the simple addition of a one-way ventilation line significantly enhance the efficiency of deoxygenation through bubbling, even approaching the effectiveness of the FPT method? To address this question, we conducted simulations for the PLEF curves, employing a hybrid approach combining a simplified kinetic model and the Stern–Volmer equation. The kinetic model considers the exchange of oxygen molecules between an  $\text{O}_2$ -containing Ar bubble and the  $\text{O}_2$ -containing solvent at the bubble–solvent interface, as illustrated in Scheme 1.

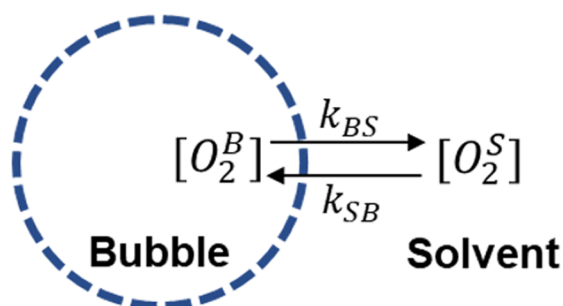
The model can be described as follows: The vast majority of the bubble's volume is occupied by Ar gas, while only a minor fraction ( $\sim 10$  ppm) contains  $\text{O}_2$  as “a contaminant”. As the Ar bubble forms at the tip of the inlet needle within the solvent, gas exchange occurs at the bubble–solvent interface, governed by Henry's law (eq 1).

$$[G^S] = \frac{x_G P}{H} \quad (1)$$

, where  $[G^S]$  represents the dissolved concentration of gas G in a solvent,  $P$  is the pressure in the gas phase of the container



### Scheme 1. A Kinetic Model for O<sub>2</sub> Exchange between an Inert Gas Bubble and Solvent<sup>a</sup>



<sup>a</sup>[O<sub>2</sub><sup>B</sup>]: O<sub>2</sub> concentration in an inert gas bubble, [O<sub>2</sub><sup>S</sup>]: O<sub>2</sub> concentration in a solvent,  $k_{BS}$ : bubble-to-solvent diffusion rate constant for O<sub>2</sub>,  $k_{SB}$ : solvent-to-bubble diffusion rate constant for O<sub>2</sub>.

(for example, a bubble and a headspace of the cuvette),  $x_G$  is the mole fraction of G in the gas phase, and  $H$  is Henry's constant. Considering the initial stage of the Ar-gas bubbling, Ar gas diffuses from the bubble into the solvent because  $x_{Ar}$  is large while  $[Ar^S]$  is small. On the other hand, the dissolved O<sub>2</sub> in the solvent diffuses into the bubble because  $x_{O_2}$  is small while  $[O_2^S]$  is large as the bubble ascends toward the surface and bursts. Subsequent bubbles, each carrying the same proportions of Ar and O<sub>2</sub>, continue to exchange gases with the solvent, which now contains less O<sub>2</sub> than before. This exchange process persists until the concentration of O<sub>2</sub> in the bubble reaches equilibrium with that in the solvent. Consequently, the final oxygen level in the solvent is influenced by the presence of the O<sub>2</sub> contaminants in the bubbling gas. In this model, we assumed that bubble–solvent gas exchange dominates over headspace–solvent gas exchange. This assumption is based on the larger surface area of the bubble–solvent interface facilitated by the rapid flow of small gas bubbles (see Supporting Video S1). Furthermore, Figure S7 shows that while headspace purging with the needle tip located above the solvent takes longer than 3500 s for full deoxygenation, bubbling achieves the same in only 150 s.

Our focus lies in tracking the variation in the oxygen content within a solvent during the bubbling process. To this end, we formulated a kinetic equation for  $[O_2^S](t)$ , the time-dependent dissolved oxygen concentration in the solvent, from the model depicted in Scheme 1:

$$\frac{d[O_2^S](t)}{dt} = k_{BS}[O_2^B](t) - k_{SB}[O_2^S](t) \quad (2)$$

$[O_2^B](t)$  denotes the oxygen concentration within a bubble, and  $k_{BS}$  and  $k_{SB}$  represent the rate constants for the diffusion of O<sub>2</sub> from the bubble to the solvent and from the solvent to the bubble, respectively. Given our experimental conditions, with the continuous introduction of fresh bubbles and their rapid

movement from the needle tip to the solvent surface, we assume that the oxygen concentration within each bubble remains effectively constant throughout the bubbling duration. We denote this constant oxygen concentration in the bubbles as  $[O_2^B]_0$ . Consequently, the equation simplifies to

$$\frac{d[O_2^S](t)}{dt} = k_{BS}[O_2^B]_0 - k_{SB}[O_2^S](t) \quad (3)$$

When  $k_{BS} = k_{SB}$ , it is reduced to a conventional mass transfer equation:<sup>44–47</sup>

$$\frac{d[O_2^S](t)}{dt} = k_{BS}([O_2^B]_0 - [O_2^S](t)) \quad (4)$$

By solving eq 3, the dissolved oxygen concentration can be expressed as

$$[O_2^S](t) = \frac{k_{BS}}{k_{SB}}[O_2^B]_0 \left(1 - \frac{1}{e^{k_{SB}t}}\right) + \frac{[O_2^S](0)}{e^{k_{SB}t}} \quad (5)$$

When fully bubbled at  $t = \infty$ ,  $[O_2^S](\infty) = \frac{k_{BS}[O_2^B]_0}{k_{SB}}$ . This behavior aligns with the plateau observed in the PLEF curves in Figure 3, indicating that  $[O_2^B](\infty)$  depends on  $[O_2^B]_0$ .

The variation in emission intensity  $I(t)$  of PtOEP\* over the bubbling time  $t$  can be described using the Stern–Volmer equation,<sup>48</sup> considering an oxygen molecule in the solvent as a quencher of PtOEP\* (Supporting Information, Section 5, for derivation):

$$PLEF(t) = \frac{I(t)}{I(0)} = \frac{1}{1 + k_q\tau_0([O_2^S](t) - [O_2^S](0))} \quad (6)$$

, where  $k_q$  denotes PtOEP's quenching rate constant by O<sub>2</sub> in the solvent and can be estimated by the experimentally measured PL lifetimes:  $k_{q,ACN} = 6.14 \times 10^4 \text{ ppm}^{-1} \text{ s}^{-1}$ ,  $k_{q,TOL} = 2.43 \times 10^4 \text{ ppm}^{-1} \text{ s}^{-1}$ .<sup>48</sup> This relationship is described by

$$\frac{1}{\tau_0} - \frac{1}{\tau^*} = k_q[O_2^S](0) \quad (7)$$

, where  $\tau^*$  is the PL lifetime of PtOEP\* in the absence of quencher O<sub>2</sub>, approximated to be that of the FPT-treated sample as measured in Figure S6, i.e.,  $\tau^* \approx \tau_{FPT}$  (104 μs for ACN and 95 μs for TOL).  $[O_2^S](0)$ , the initial oxygen concentration in the solvent, is obtained as 90.8 and 179.1 ppm for ACN and TOL, using Henry's law (eq 1), where  $P$  was measured to be 1.031 bar during air bubbling,  $x_{O_2}$  is the mole fraction of O<sub>2</sub> in ambient air (0.2095), and  $H = 2378$  and 1206 bar for ACN and TOL at 20 °C, respectively.<sup>49,50</sup> Substituting eq 5 with eq 6 yields

$$PLEF(t) = \frac{1}{1 + k_q\tau_0 \left( \frac{k_{BS}}{k_{SB}}[O_2^B]_0 \left(1 - \frac{1}{e^{k_{SB}t}}\right) + \frac{[O_2^S](0)}{e^{k_{SB}t}} - [O_2^S](0) \right)} \quad (8)$$

Table 1. Results of Fitting the PLEF Profiles ( $n = 3$ , Figure S2) with Eq 8<sup>a</sup>

Solvent	$k_{SB} (\times 10^{-2} \text{ s}^{-1})$	$k_{BS}[O_2^B]_0 (\times 10^{-3} \text{ ppm s}^{-1})$ at $R_{vent} =$					
		0 sccm <sup>b</sup>	50 sccm	100 sccm	200 sccm	300 sccm	400 sccm
ACN	7.41 ± 0.29	3.78 ± 0.29	1.49 ± 0.06	1.07 ± 0.07	0.94 ± 0.05	0.88 ± 0.06	0.81 ± 0.09
TOL	6.97 ± 0.36	5.22 ± 0.56	3.23 ± 0.59	2.92 ± 0.69	2.22 ± 0.55	1.95 ± 0.25	1.78 ± 0.15

<sup>a</sup>See Supporting Information Section 6 for details. PLEF: photoluminescence enhancement factor. <sup>b</sup>Condition equivalent to the conventional setup.

This equation was used to fit the PLEF curves presented in Figure S2, and the values of the two fitting parameters,  $k_{BS}[O_2^B]_0$  and  $k_{SB}$ , are summarized in Tables 1, S5, and S6 (Supporting Information, Section 6 for details). The nearly identical normalized PLEF profiles in a given solvent (Figure S3) suggest consistent deoxygenation dynamics, regardless of  $R_{vent}$ . Consequently,  $k_{BS}$  and  $k_{SB}$  can be considered invariant with respect to  $R_{vent}$ . Throughout the fitting process,  $k_{SB}$  was assumed to be constant, yielding values of  $(7.41 \pm 0.29) \times 10^{-2} \text{ s}^{-1}$  for ACN and  $(6.97 \pm 0.36) \times 10^{-2} \text{ s}^{-1}$  for TOL. The invariant  $k_{BS}$  suggests that  $[O_2^B]_0$  decreases with increasing  $R_{vent}$  as the product  $k_{BS}[O_2^B]_0$  decreases with increasing  $R_{vent}$ . This indicates that the one-way ventilation line effectively mitigates  $O_2$  contamination in the Ar bubble. There are three potential sources of oxygen contamination: (1) the high oxygen gas permeability of Teflon tubing,<sup>6</sup> (2) tube-to-tube and tube-to-MFC joints, and (3) desorption of the oxygen molecules adsorbed onto tubing walls by Ar gas flow. Sources (1) and (2) are plausible given the significant oxygen concentration in ambient air ( $2.1 \times 10^6$  ppm) compared to the tens of ppm of oxygen in 99.999% pure Ar gas at similar pressures, a difference spanning 5 orders of magnitude. These two sources can be addressed by using metal tubing with lower oxygen permeability and by improving the precision of tube fittings. Source (3) can be mitigated by flushing the entire tubing with Ar gas and/or baking the tubing under vacuum prior to the deoxygenation process. Identifying the exact source of contamination would be informative and a valuable direction for future, more comprehensive investigation.

As  $[O_2^B]_0$  is typically in the range of tens of ppm, the magnitude of  $k_{BS}$  lies between  $10^{-4}$  and  $10^{-5} \text{ s}^{-1}$ , which is 2 to 3 orders of magnitude smaller than that of  $k_{SB}$ . This means that oxygen molecules diffuse so efficiently from the solvent into the bubbles that the continuously supplied Ar gas bubbles can effectively extract oxygen from the solvent. Another notable aspect of the  $k_{BS}[O_2^B]_0$  is that it exhibits a higher value in TOL than in ACN by a factor of 1.3–2.6 (Table 1). Given that  $[O_2^B]_0$  is constant at a given value of  $R_{vent}$ , this discrepancy reflects the variation in  $k_{BS}$  in different solvents; in other words,  $k_{BS,TOL} > k_{BS,ACN}$ . This result, together with  $k_{SB,TOL} < k_{SB,ACN}$  in Table 1, aligns well with the higher  $O_2$  solubility in TOL compared to ACN.

Based on these observations and analyses, we conclude that the addition of a one-way ventilation pathway serves to reduce  $[O_2^B]_0$  by increasing the Ar gas flow rate within the tube between the regulator and the ventilation outlet (Figure 1b). Without the ventilation path (i.e.,  $R_{vent} = 0$  sccm), the flow rate relies solely on the flow rate into the sample cuvette through the needle set by  $R_{in} = 20$  sccm. The slow flow rate within the tube allows for a greater chance of external  $O_2$  leak-in, resulting in high  $O_2$  contamination within the Ar bubble. However, when ventilation is activated (e.g.,  $R_{vent} = 400$  sccm and  $R_{in} = 20$  sccm), the flow rate of Ar gas within the tube increases, thereby reducing the amount of leak-in of  $O_2$  per unit volume of Ar gas. Consequently, Ar gas with minimized levels of contamination with  $O_2$  is supplied to the solvent, making deoxygenation more efficient.

### 3. CONCLUSIONS

In conclusion, this study introduces an enhanced inert gas bubbling method for solvent deoxygenation by incorporating a one-way ventilation path alongside an Ar gas inlet needle. The method, characterized by its simplicity, speed, and cost-

effectiveness, notably improves deoxygenation efficiency as evidenced by 26.0% and 12.1% enhancement in PLEF values for ACN and TOL, compared to the conventional bubbling setup. This achievement corresponds to up to 94% of the rigorous freeze–pump–thaw method, validating the efficacy of the proposed method. The result was further supported by PL lifetime measurements, which confirmed the absence of concentration-dependent artifacts in the PL intensity-based assessment.

The profiles of  $PLEF(R_{vent}, t)$  were simulated utilizing a simplified kinetic model and the Stern–Volmer equation, treating oxygen molecules as dynamic quenchers of luminescent PtOEP\*. The fitting parameters,  $k_{SB}$  and  $k_{BS}[O_2^B]_0$ , indicate that the initial concentration of oxygen in the inert gas bubble  $[O_2^B]_0$  decreases with an increasing ventilation flow rate,  $R_{vent}$ . Our experimental observations, coupled with the simulation results, elucidate the pivotal role of the added ventilation pathway in the enhancement of deoxygenation. Specifically, increased ventilation increases the inert gas flow rate within the tube connecting the regulator and the inlet needle, thereby reducing the likelihood of the bubbling gas being contaminated by an  $O_2$  leak-in. Consequently, this reduces the  $O_2$  contamination within the inert gas bubble formed at the needle tip. Additionally, the fitting results, which yield higher values of  $k_{BS}$  (the bubble-to-solvent diffusion rate constant for  $O_2$ ) for TOL compared to those for ACN and lower values of  $k_{SB}$  (the solvent-to-bubble diffusion rate constant for  $O_2$ ) for TOL than ACN, are in good agreement with the fact that oxygen exhibits higher solubility in TOL than in ACN. Although the simulation model employed herein offers utility, its simplicity may inadvertently overlook certain nuances. Therefore, it would be advisable to employ more sophisticated and rigorous theoretical methodologies for further investigation.

The method outlined in this study holds promise for applications across diverse academic and industrial domains that necessitate consistent and efficient solvent deoxygenation with minimal setup complexity and safety concerns. Moreover, this method is easily applicable to both aqueous and biological samples, and it can be readily scaled up for larger applications.

While the improved bubbling method introduced in this study offers enhanced deoxygenation efficiency, it is important to recognize that this improvement comes with a trade-off: increased gas consumption due to the addition of the ventilation pathway. To reduce this cost, we propose using nitrogen ( $N_2$ ) gas instead of argon (Ar), making it a more cost-effective choice for many applications without compromising the performance of the deoxygenation. Additionally, optimizing the system with less permeable tubing and high-quality fittings can further reduce  $O_2$  contamination, resulting in a more efficient overall process. These relatively simple adjustments can substantially lower operating costs, making the method more scalable and practical for a variety of applications. Although gas consumption may be higher in this setup, it is essential to weigh these expenses against the potential for improved product quality. The enhanced deoxygenation efficiency of the new method can lead to higher-quality final products, potentially offsetting the additional gas costs. This balance between operational cost and product quality makes the new method particularly attractive for applications in which product performance is critical. The preliminary discussion provided here highlights the key economic and practical factors of the proposed method.

Future studies will aim to conduct a more detailed technoeconomic analysis, considering energy consumption, cost-effectiveness, and scalability, to fully assess the broader implications of this improved setup.

#### 4. METHODS

**Sample Preparation.** Platinum(II) octaethylporphyrin was purchased from Merck, and HPLC-grade acetonitrile and toluene were purchased from Fisher Scientific. All chemicals were used without further purification. All measurements were performed by using 5  $\mu$ M PtOEP solutions.

**An Improved Bubbling Setup.** Ultrapure Ar gas (99.999%, Deaduk Gas, Gunsan, Korea) was regulated to provide a slightly higher pressure than ambient pressure, approximately 1.4 bar, to the subsequent combination of 1/4 in. stainless steel and Teflon tubing. The inlet flow rate ( $R_{in}$ ) from the needle to the solvent was set at 20 sccm using a mass flow controller (MC-100SCCM-D-TC, Alicat Scientific). The ventilation rate ( $R_{vent}$ ) was precisely controlled by another MFC (MCS-500SCCM-D-DB15-485-TC, Alicat Scientific). A 3 mL solution was prepared in a quartz cuvette (3Q10-GL14-S, 1 cm  $\times$  1 cm, Starna), which was then screw-capped with a silicone septum to minimize solvent volume changes due to evaporation during bubbling. A 20G inlet needle was inserted into the solvent in the cuvette through the silicone septum, while another short needle was positioned in the headspace above the solvent through the septum to prevent pressure buildup. Prior to each measurement, the solution was fully air saturated by bubbling from an air bubbler for 5 min.

**Steady-State Spectroscopy.** The absorption and PL spectra were obtained using a UV–vis spectrometer (Ultraspec 2100 Pro, Biochrom US) and a fluorometer (FLS980, Edinburgh Instruments), respectively.

**Real-Time Monitoring of Photoluminescence Enhancement Factor.** As depicted in Figure S1a, a sample was excited by a 15  $\mu$ W 355 nm continuous-wave laser (Cobolt Zouk, Hübner Photonics), and the emission of the sample was collected through the polished bottom of the cuvette. It was then steered by a liquid light guide (LLG0538-8, Thorlabs) into the detection module of the fluorometer (FLS980, Edinburgh Instruments) after passing through a 590 nm long-pass filter and recorded in kinetic mode at 650 nm. All measurements were made at least three times to ensure reproducibility.

**Time-Resolved Spectroscopy.** For PL lifetime measurement, samples were irradiated utilizing the third harmonics (355 nm) of a Nd:YAG pulsed laser (Q-Smart450, Quantel Laser) with an approximate pulse length of 6 ns and operating at 10 Hz frequency. The laser beam was delivered to the sample via an optical fiber (FP1500URT, Thorlabs), maintaining a power of 15  $\mu$ W at the position of the sample. Emission was collected from the bottom of the cuvette using the same liquid light guide and directed to a preamplified photomultiplier tube (PMT) (H11526-NF, Hamamatsu) passing through a 650 nm bandpass filter (40 nm fwhm). The PMT signal was then transmitted to a digital oscilloscope (TDS3054B, Tektronix) controlled by LabVIEW software running on a PC (Figure S1b).

**Preparation for Freeze–Pump–Thaw-Treated Samples.** As a reference, we prepared samples treated with FPT cycles, and their deoxygenation efficiencies were subsequently compared with those treated using the enhanced Ar gas bubbling method of this work. The FPT-treated samples

underwent multiple (more than three) cycles until pressure stabilization was achieved at approximately  $10^{-5}$  Torr.

#### ■ ASSOCIATED CONTENT

##### Supporting Information


The Supporting Information is available free of charge at <https://pubs.acs.org/doi/10.1021/acsomega.4c05786>.

Detailed experimental methods, real-time photoluminescence enhancement factor data, photoluminescence lifetime data, comparison of bubbling and headspace purging methods by PLEF measurement, derivation for eq 6, PLEF curve fitting procedure (PDF)

A video showing Ar gas bubbling at 20 sccm flow rate in toluene (MP4)

#### ■ AUTHOR INFORMATION

##### Corresponding Author

Hohjai Lee – Department of Chemistry, Gwangju Institute of Science and Technology (GIST), Gwangju 61005, South Korea; Innovative Energy and Carbon Optimized Synthesis for Chemicals (Inn-ECOSysChem) Research Center (ERC), Gwangju 61005, South Korea;  [orcid.org/0000-0002-6810-0206](https://orcid.org/0000-0002-6810-0206); Email: [hohjai@gist.ac.kr](mailto:hohjai@gist.ac.kr)

##### Authors

Dongcheol Park – Department of Chemistry, Gwangju Institute of Science and Technology (GIST), Gwangju 61005, South Korea; Innovative Energy and Carbon Optimized Synthesis for Chemicals (Inn-ECOSysChem) Research Center (ERC), Gwangju 61005, South Korea

Seong Min Won – Department of Chemistry, Gwangju Institute of Science and Technology (GIST), Gwangju 61005, South Korea; Innovative Energy and Carbon Optimized Synthesis for Chemicals (Inn-ECOSysChem) Research Center (ERC), Gwangju 61005, South Korea

Complete contact information is available at: <https://pubs.acs.org/10.1021/acsomega.4c05786>

##### Notes

The authors declare no competing financial interest.

#### ■ ACKNOWLEDGMENTS

This work was supported by the National Research Foundation of Korea (NRF) grant funded by the Korean government (MSIT) (No. 2021R1A5A1028138) and Samsung Science and Technology Foundation under Project Number SSTF-BA2002-10.

#### ■ REFERENCES

- (1) Bertram, C.; Hass, R. Cellular responses to reactive oxygen species-induced DNA damage and aging. *Biol. Chem.* **2008**, 389, 211–220.
- (2) Pole, A.; Dimri, M.; Dimri, G. P. Oxidative stress, cellular senescence and ageing. *AIMS Mole. Sci.* **2016**, 3, 300–324.
- (3) Sies, H.; Jones, D. P. Reactive oxygen species (ROS) as pleiotropic physiological signalling agents. *Nat. Rev. Mol. Cell Biol.* **2020**, 21, 363–383.
- (4) Dzebo, D.; Moth-Poulsen, K.; Albinsson, B. Robust triplet–triplet annihilation photon upconversion by efficient oxygen scavenging. *Photochem. Photobiol. Sci.* **2017**, 16, 1327–1334.
- (5) Barboy, N.; Feitelson, J. Deoxygenation of solutions for transient studies. *Anal. Biochem.* **1989**, 180, 384–386.



- (6) Baronas, P.; Elholm, J. L.; Moth-Poulsen, K. Efficient degassing and ppm-level oxygen monitoring flow chemistry system. *React. Chem. Eng.* **2023**, *8*, 2052–2059.
- (7) Rollié, M. E.; Patonay, G.; Warner, I. M. Deoxygenation of solutions and its analytical applications. *Ind. Eng. Chem. Res.* **1987**, *26*, 1–6.
- (8) Pynaert, R.; Buguet, J.; Croutxé-Barghorn, C.; Moireau, P.; Allonas, X. Effect of reactive oxygen species on the kinetics of free radical photopolymerization. *Polym. Chem.* **2013**, *4*, 2475–2479.
- (9) O'Brien, A. K.; Bowman, C. N. Impact of oxygen on photopolymerization kinetics and polymer structure. *Macromolecules* **2006**, *39*, 2501–2506.
- (10) Yao, X.; Dong, Q.; Cheng, Q.; Wang, D. Why do lithium–oxygen batteries fail: parasitic chemical reactions and their synergistic effect. *Angew. Chem., Int. Ed.* **2016**, *55*, 11344–11353.
- (11) Lee, H.; Yang, N.; Cohen, A. E. Mapping nanomagnetic fields using a radical pair reaction. *Nano Lett.* **2011**, *11*, 5367–5372.
- (12) Lee, H.; Brinks, D.; Cohen, A. E. Two-photon imaging of a magneto-fluorescent indicator for 3D optical magnetometry. *Opt. Express* **2015**, *23*, 28022–28030.
- (13) Kim, D.; Jung, M.; Kim, H.; Chung, W.-j.; Lee, H. Quantitative imaging of magnetic field distribution using a pyrene-based magnetosensing exciplex fluorophore. *Photochem. Photobiol. Sci.* **2019**, *18*, 2688–2695.
- (14) Kim, D.; Lee, Y. J.; Ahn, D.-H.; Song, J.-W.; Seo, J.; Lee, H. Peptoid-conjugated magnetic field-sensitive exciplex system at high and low solvent polarities. *J. Phys. Chem. Lett.* **2020**, *11*, 4668–4677.
- (15) Magano, J.; Dunetz, J. R. Large-scale applications of transition metal-catalyzed couplings for the synthesis of pharmaceuticals. *Chem. Rev.* **2011**, *111*, 2177–2250.
- (16) Besson, M.; Gallezot, P. Deactivation of metal catalysts in liquid phase organic reactions. *Catal. Today* **2003**, *81*, 547–559.
- (17) Kumar, K.; Dubau, L.; Mermoux, M.; Li, J.; Zitolo, A.; Nelayah, J.; Jaouen, F.; Maillard, F. On the influence of oxygen on the degradation of Fe–N–C catalysts. *Angew. Chem., Int. Ed.* **2020**, *59*, 3235–3234.
- (18) Li, H.; Buesen, D.; Dementin, S.; Léger, C.; Fourmond, V.; Plumere, N. Complete protection of O<sub>2</sub>-sensitive catalysts in thin films. *J. Am. Chem. Soc.* **2019**, *141*, 16734–16742.
- (19) Ware, W. R. Oxygen quenching of fluorescence in solution: an experimental study of the diffusion process. *J. Phys. Chem.* **1962**, *66*, 455–458.
- (20) Zheng, Q.; Jockusch, S.; Zhou, Z.; Blanchard, S. C. The contribution of reactive oxygen species to the photobleaching of organic fluorophores. *Photochem. Photobiol.* **2014**, *90*, 448–454.
- (21) Demchenko, A. P. Photobleaching of organic fluorophores: quantitative characterization, mechanisms, protection. *Methods Appl. Fluoresc.* **2020**, *8*, No. 022001.
- (22) Mehmood, F.; Pachter, R.; Lu, W.; Boeckl, J. J. Adsorption and diffusion of oxygen on single-layer graphene with topological defects. *J. Phys. Chem. C* **2013**, *117*, 10366–10374.
- (23) Xu, X.; Zhuang, J.; Du, Y.; Feng, H.; Zhang, N.; Liu, C.; Lei, T.; Wang, J.; Spencer, M.; Morishita, T.; Wang, X.; Dou, S. X. Effects of oxygen adsorption on the surface state of epitaxial silicene on Ag (111). *Sci. Rep.* **2014**, *4*, 7543.
- (24) Rizzo, A.; Signore, M. A.; Valerini, D.; Altamura, D.; Cappello, A.; Tapfer, L. A study of suppression effect of oxygen contamination by bias voltage in reactively sputtered ZrN films. *Surf. Coat. Technol.* **2012**, *206*, 2711–2718.
- (25) Merritt, J. M.; Buser, J. Y.; Campbell, A. N.; Fennell, J. W.; Kallman, N. J.; Koenig, T. M.; Moursy, H.; Pietz, M. A.; Scully, N.; Singh, U. K. Use of modeling and process analytical technologies in the design of a catalytic amination reaction: understanding oxygen sensitivity at the lab and manufacturing scales. *Org. Process Res. Dev.* **2014**, *18*, 246–256.
- (26) He, S.; Wong, J.; Inn, D.; Hoex, B.; Aberle, A. G.; Sproul, A. B. Influences of oxygen contamination on evaporated poly-Si thin-film solar cells by solid-phase epitaxy. *Thin Solid Films* **2010**, *518*, 4351–4355.
- (27) Sudheendran Swayamprabha, S.; Dubey, D. K.; Shah Nawaz; Yadav, R. A. K.; Nagar, M. R.; Sharma, A.; Tung, F.-C.; Jou, J.-H. Approaches for long lifetime organic light emitting diodes. *Adv. Sci.* **2021**, *8*, No. 2002254.
- (28) Aziz, H.; Popovic, Z. D. Degradation phenomena in small-molecule organic light-emitting devices. *Chem. Mater.* **2004**, *16*, 4522–4532.
- (29) Scholz, S.; Kondakov, D.; Lüssem, B.; Leo, K. Degradation mechanisms and reactions in organic light-emitting devices. *Chem. Rev.* **2015**, *115*, 8449–8503.
- (30) Grossiord, N.; Kroon, J. M.; Andriessen, R.; Blom, P. W. M. Degradation mechanisms in organic photovoltaic devices. *Org. Electron.* **2012**, *13*, 432–456.
- (31) Pan, T.; Liu, S.; Zhang, L.; Xie, W. Flexible organic optoelectronic devices on paper. *iScience* **2022**, *25*, No. 103782.
- (32) Schaer, M.; Nüesch, F.; Berner, D.; Leo, W.; Zuppiroli, L. Water vapor and oxygen degradation mechanisms in organic light emitting diodes. *Adv. Funct. Mater.* **2001**, *11*, 116–121.
- (33) Brenner, P.; Fleig, L.-M.; Liu, X.; Welle, A.; Bräse, S.; Lemmer, U. Degradation mechanisms of polyfluorene-based organic semiconductor lasers under ambient and oxygen-free conditions. *J. Polym. Sci., Part B: Polym. Phys.* **2015**, *53*, 1029–1034.
- (34) Butler, I. B.; Schoonen, M. A. A.; Rickard, D. T. Removal of dissolved oxygen from water: A comparison of four common techniques. *Talanta* **1994**, *41*, 211–215.
- (35) Borys, A. M. An illustrated guide to Schlenk line techniques. *Organometallics* **2023**, *42*, 182–196.
- (36) Pagano, T.; Biacchi, A. J.; Kenny, J. E. Nitrogen gas purging for the deoxygenation of polyaromatic hydrocarbon solutions in cyclohexane for routine fluorescence analysis. *Appl. Spectrosc.* **2008**, *62*, 333–336.
- (37) Aitken, C. E.; Marshall, R. A.; Puglisi, J. D. An oxygen scavenging system for improvement of dye stability in single-molecule fluorescence experiments. *Biophys. J.* **2008**, *94*, 1826–1835.
- (38) Jung, S.-R.; Deng, Y.; Kushmerick, C.; Asbury, C. L.; Hille, B.; Koh, D.-S. Minimizing ATP depletion by oxygen scavengers for single-molecule fluorescence imaging in live cells. *Proc. Natl. Acad. Sci. U.S.A.* **2018**, *115*, E5706–E5715.
- (39) Andrew, T. L.; Swager, T. M. Reduced photobleaching of conjugated polymer films through small molecule additives. *Macromolecules* **2008**, *41*, 8306–8308.
- (40) Gaikwad, K. K.; Singh, S.; Lee, Y. S. Oxygen scavenging films in food packaging. *Environ. Chem. Lett.* **2018**, *16*, 523–538.
- (41) Pagano, T.; Carcamo, N.; Kenny, J. E. Investigation of the fluorescence quenching of 1-aminoanthracene by dissolved oxygen in cyclohexane. *J. Phys. Chem. A* **2014**, *118*, 11512–11520.
- (42) Bansal, A. K.; Holzer, W.; Penzkofer, A.; Tsuboi, T. Absorption and emission spectroscopic characterization of platinum-octaethylporphyrin (PtOEP). *Chem. Phys.* **2006**, *330*, 118–129.
- (43) Bakalyar, S. R.; Bradley, M. P. T.; Horganen, R. The role of dissolved gases in high-performance liquid chromatography. *J. Chromatogr. A* **1978**, *158*, 277–293.
- (44) Lewis, W. K.; Whitman, W. G. Principles of Gas Absorption. *Ind. Eng. Chem.* **1924**, *16*, 1215–1220.
- (45) Villadsen, J.; Nielsen, J.; Lidén, G. *Bioreaction Engineering Principles*, 3rd ed.; Springer: Boston, 2011.
- (46) Buser, J. Y.; Luciani, C. V. A new method for determination of gas–liquid mass transfer coefficients by direct measurement of gas uptake by flow NMR. *React. Chem. Eng.* **2018**, *3*, 442–446.
- (47) Kawahara, A.; Sadatomi, M.; Matsuyama, F.; Matsuura, H.; Tominaga, M.; Noguchi, M. Prediction of micro-bubble dissolution characteristics in water and seawater. *Exp. Therm. Fluid Sci.* **2009**, *33*, 883–894.
- (48) Lakowicz, J. R. *Principles of Fluorescence Spectroscopy*, 3<sup>rd</sup> ed.; Springer: Boston, 2006.
- (49) Lawrence Clever, H.; Battino, R.; Miyamoto, H.; Yampolski, Y.; Young, C. L. IUPAC-NIST solubility data series. 103. Oxygen and ozone in water, aqueous solutions, and organic liquids (supplement to

solubility data series volume 7). *J. Phys. Chem. Ref. Data* **2014**, 43, No. 033102.

(50) Wu, X.; Deng, Z.; Yan, J.; Zhang, Z.; Zhang, F.; Zhang, Z. Experimental investigation on the solubility of oxygen in toluene and acetic acid. *Ind. Eng. Chem. Res.* **2014**, 53, 9932–9937.